



**HAL**  
open science

## **Magnetic bioactive glass nano-heterostructures: a deeper insight into magnetic hyperthermia properties in the scope of bone cancer treatment**

Florestan Vergnaud, Xavier Kesse, Aurélie Jacobs, Francis Perton, Sylvie Begin-Colin, Damien Mertz, Stéphane Descamps, Charlotte Vichery, Jean-Marie Nedelec

### ► **To cite this version:**

Florestan Vergnaud, Xavier Kesse, Aurélie Jacobs, Francis Perton, Sylvie Begin-Colin, et al.. Magnetic bioactive glass nano-heterostructures: a deeper insight into magnetic hyperthermia properties in the scope of bone cancer treatment. *Biomaterials Science*, 2022, 10 (14), pp.3993-4007. 10.1039/D2BM00319H. hal-03735442

**HAL Id: hal-03735442**

**<https://uca.hal.science/hal-03735442>**

Submitted on 26 Jun 2023

**HAL** is a multi-disciplinary open access archive for the deposit and dissemination of scientific research documents, whether they are published or not. The documents may come from teaching and research institutions in France or abroad, or from public or private research centers.

L'archive ouverte pluridisciplinaire **HAL**, est destinée au dépôt et à la diffusion de documents scientifiques de niveau recherche, publiés ou non, émanant des établissements d'enseignement et de recherche français ou étrangers, des laboratoires publics ou privés.

# Magnetic bioactive glass nano-heterostructures: a deeper insight into magnetic hyperthermia properties in the scope of bone cancer treatment

Florestan Vergnaud,<sup>a</sup> Xavier Kesse,<sup>a</sup> Aurélie Jacobs,<sup>a</sup> Francis Pertont,<sup>b</sup> Sylvie Begin-Colin,<sup>b</sup> Damien Mertz,<sup>b</sup> Stéphane Descamps,<sup>c</sup> Charlotte Vichery,<sup>\*a</sup> Jean-Marie Nedelec<sup>a</sup>

<sup>a</sup> Université Clermont Auvergne, Clermont Auvergne INP, CNRS, ICCF, F-63000 Clermont-Ferrand, France.

<sup>b</sup> Institut de Physique et Chimie des Matériaux de Strasbourg (IPCMS), UMR-7504 CNRS-Université de Strasbourg, Strasbourg 67034 Cedex 2, France

<sup>c</sup> Université Clermont Auvergne, Clermont Auvergne INP, CHU de Clermont-Ferrand, CNRS, ICCF, F-63000 Clermont-Ferrand, France.

\* Corresponding author: charlotte.vichery@sigma-clermont.fr

## Abstract

Primary bone cancers commonly involve surgery to remove the malignant tumor, complemented with a postoperative treatment to prevent cancer resurgence. Studies on magnetic hyperthermia, used as a single treatment or in synergy with chemo- or radiotherapy, have shown remarkable success in the past decades. Multifunctional biomaterials with bone healing ability coupled with hyperthermia property could thus be of great interest to repair critical bone defects resulting from tumor resection. For this purpose, we designed superparamagnetic and bioactive nanoparticles (NPs) based on iron oxide cores ( $\gamma$ -Fe<sub>2</sub>O<sub>3</sub>) encapsulated in a bioactive glass (SiO<sub>2</sub>-CaO) shell. Nanometric heterostructures (122 ± 12 nm) were obtained through a two-step process: co-precipitation of 16 nm sized iron oxide NPs, followed by the growth of a bioactive glass shell *via* a modified Stöber method. Their bioactivity was confirmed by hydroxyapatite growth in simulated body fluid, and cytotoxicity assays showed they induced no significant death of human mesenchymal stem cells after 7 days. Calorimetric measurements were carried out under a wide range of alternating magnetic field amplitudes and frequencies, considering clinically relevant parameters, and some were made in viscous medium (agar) to mimic the implantation conditions. The experimental specific loss power was predictable with respect to the Linear Response Theory, and showed a maximal value of 767 ± 77 W/g<sub>Fe</sub> (769 kHz, 23.9 kA/m in water). An interesting value of 166 ± 24 W/g<sub>Fe</sub> was obtained under clinically relevant conditions (157 kHz, 23.9 kA/m) for the heterostructures immobilized in agar. The good biocompatibility, bioactivity and heating ability suggest that these  $\gamma$ -Fe<sub>2</sub>O<sub>3</sub>@SiO<sub>2</sub>-CaO NPs are a promising biomaterial to be used as it is or included in a scaffold to heal bone defects resulting from bone tumor resection.

## Introduction

One of the major challenges of the 21<sup>st</sup> century is the treatment of cancer, which despite numerous technological and clinical advances is still one of the leading causes of death in the world.<sup>1</sup> Malignant tumors can develop in one organ – breast and lungs being the main ones in 2021 according to the World Health Organization – but if not detected early, cancerous cells can spread and develop metastases in other parts of the body. Among the organs affected, bones are one of the privileged sites, with 70 % of breast and prostate cancers and 30–40 % of thyroid, kidney and lung cancers resulting in bone metastatic tumors.<sup>2</sup> Even if primary bone tumors such as osteosarcoma, chondrosarcoma or Ewing sarcoma concern about 3 % of the cases of children and adolescent cancers and less than 1 % in adults, it still has an estimated incidence of 4.8 per million patients annually.<sup>3</sup> In the case of primary bone tumors, as the survival rates are low if only chemotherapy or radiotherapy is applied, one of the very first response is surgery.<sup>4</sup> Moreover, postoperative chemotherapy and/or radiotherapy are needed to prevent cancer recurrence or metastases, bringing their drawbacks and side effects. Due to the physiological differences between cancerous and healthy cells, malignant cells are more sensitive to heat, and a temperature above 41 °C induces cytotoxic effects, while a temperature above 46 °C is needed to destroy healthy cells by thermoablation.<sup>5,6</sup> Therefore, hyperthermia is seen as a promising tumor

therapy, as a local temperature rise could be used to selectively treat cancer cells without damaging surrounding tissues. In the case of bone tumors, hyperthermia could also promote bone regeneration, as it has been shown that heat in this range of temperature can stimulate osteogenesis *in vivo*.<sup>7</sup>

The first use of magnetic particles for cancer treatment by hyperthermia is reported in 1957 by Gilchrist *et al.*<sup>8</sup> Since then, a growing body of research focused on the development and study of magnetic thermoseeds that can provide effective heating of deep-seated tumors under the influence of a locally applied magnetic field. In addition to their use as a single treatment, many studies, including clinical trials, demonstrated an improved efficiency with no additional toxicity when standard cancer treatments were coupled with hyperthermia.<sup>5,9-11</sup> Indeed, magnetic hyperthermia (MH) can be a valuable ally in the fight against cancer as a synergistic treatment, through thermal chemosensitization<sup>12,13</sup> and radiosensitization at mild temperatures (39–42 °C).<sup>11,14,15</sup> Superparamagnetic iron oxide nanoparticles (SPIONs) are frequently considered as the best choice for medical applications, as they have excellent MH response under alternating magnetic field (AMF), by generating heat thanks to magnetic relaxation mechanisms. In addition, they present a high saturation magnetization, a zero net magnetization in the absence of a magnetic field, and are biocompatible.<sup>16</sup> Moreover, the human body is well equipped to metabolize iron.<sup>17</sup> The materials most commonly used are magnetite (Fe<sub>3</sub>O<sub>4</sub>) and maghemite (γ-Fe<sub>2</sub>O<sub>3</sub>) nanoparticles, which are superparamagnetic for diameters below 30 nm. These SPIONs are already commercialized and approved by the US Food and Drug Administration (FDA) as Magnetic Resonance Imaging (MRI) contrast agents or delivery agents (Feridex®, Feraheme®, Gastromark®...) and more recently approved by the European Medicines Agency (EMA) for the magnetic hyperthermia treatment NanoTherm® from MagForce (Germany).<sup>18</sup>

In the case of bone cancer, the tumor resection generally results in a critical-size defect that cannot be repaired by the natural bone regeneration processes, and thus requires a bone graft. The development of synthetic graft materials allowed to overcome graft availability or rejection issues, these being the main drawbacks of autografts or allografts. Bioactive glass (BG) is an attractive material thanks to its ability to react in biological media and form a hydroxyapatite layer onto its surface, whose composition is similar to the one of the mineral part of bones. The implanted material can thus strongly bond with surrounding tissues and enhance bone repair. Also, BG dissolution products are known to provide osteogenic properties.<sup>19</sup> Since the original Hench's 45S5 Bioglass® obtained through a melt-quenching route in the 1970s,<sup>20</sup> several studies focused on sol-gel bioactive glasses.<sup>19,21</sup> In addition to the lower temperature required for their synthesis, chemical and morphological properties of sol-gel BGs can be finely tuned to affect biological responses. Indeed, as they can present some porosity and be nanosized, they show a high specific surface area which enhances their mineralization kinetics. Even simple systems such as binary (SiO<sub>2</sub>-CaO) BGs synthesized with this method have shown excellent bioactivity properties.<sup>22</sup> Moreover, BGs can be doped during their synthesis with elements that can stimulate osteogenesis (*e. g.* P, Mg, Zn), angiogenesis (*e. g.* Cu), anti-inflammatory effects (Zn, Sr) and antibacterial effects (Ag, Cu).<sup>23,24</sup>

Hence, a multifunctional bone substitute, that both promotes bone regeneration and enables a local hyperthermia treatment of cancer is of high clinical interest. As the material would bond with bone tissues, the SPIONs embedded in the bioactive material would stay at the implantation site and would be available for successive hyperthermia treatments. Moreover, several studies have shown that the presence of SPIONs in the biomaterial stimulates alkaline phosphatase (ALP) activity, osteogenic gene expression, proliferation, differentiation of human bone marrow stem cells and extracellular matrix mineralization, and thus allowed a faster bone regeneration, even without the application of AMF.<sup>25,26</sup> A multifunctional magnetic bioactive glass-ceramic was first developed in 1991 by Ohura *et al.* and showed the ability to bond with bone tissues and to provide local heating under AMF.<sup>27</sup> Their interesting bone tumor treatment results in rabbits acted as a proof of concept for this therapy.<sup>28</sup> However, this material was synthesized through a one-pot melting route that provided poor control on the crystallinity and properties of the magnetic phase. Matsumine *et al.* presented good clinical results with a Fe<sub>3</sub>O<sub>4</sub> nanopowder mixed with calcium phosphate cement on human patients with metastatic bone lesions by hyperthermia treatment, indicating that a SPIONs-containing bone substitute is a promising approach for a treatment after bone tumor surgery.<sup>29</sup>

In this work, a magnetic and bioactive multifunctional nanomaterial based on SPIONs ( $\gamma\text{-Fe}_2\text{O}_3$ ) as a core and BG ( $\text{SiO}_2\text{-CaO}$ ) as a shell is presented. These heterostructured nanoparticles (NPs) were synthesized through a co-precipitation and sol-gel approach based on our previous work.<sup>30</sup> The different steps of the core-shell NPs synthesis are depicted in Fig. 1. As optimal maghemite NPs size for MH is reported as between 14 and 16 nm, the synthesis protocol was adapted to improve heating efficiency.<sup>6</sup> In addition to the morphological, structural and magnetic properties, as well as the bioactivity and cytocompatibility assessments, we particularly focused on a deeper study of the magnetic hyperthermia response of these heterostructures. As they are intended for medical applications, MH measurements were carried out under clinically relevant AMF parameters and in viscous medium, in order to work closer to *in vivo* conditions. The specific loss power (SLP) behavior is compared to a theoretical model in order to predict its values under different AMF frequencies and amplitudes, and obtained intrinsic loss power (ILP) values are discussed.

By providing extensive information about the MH behavior of this nanomaterial, we believe it can be easily compared with similar systems from the literature and eventually used as a building block for bone filling material after bone tumor surgery. The nanometric size of this material indeed allows a high versatility of material shaping: they can be dispersed in polymer,<sup>31</sup> hydrogel,<sup>32,33</sup> calcium phosphate cement<sup>34,35</sup> and/or shaped as scaffold (*via* 3D-printing,<sup>36-38</sup> electrospinning<sup>39,40</sup> or foam replica<sup>41</sup>), or directly mixed with patient blood. The considered therapeutic approach is illustrated in Fig. 1.

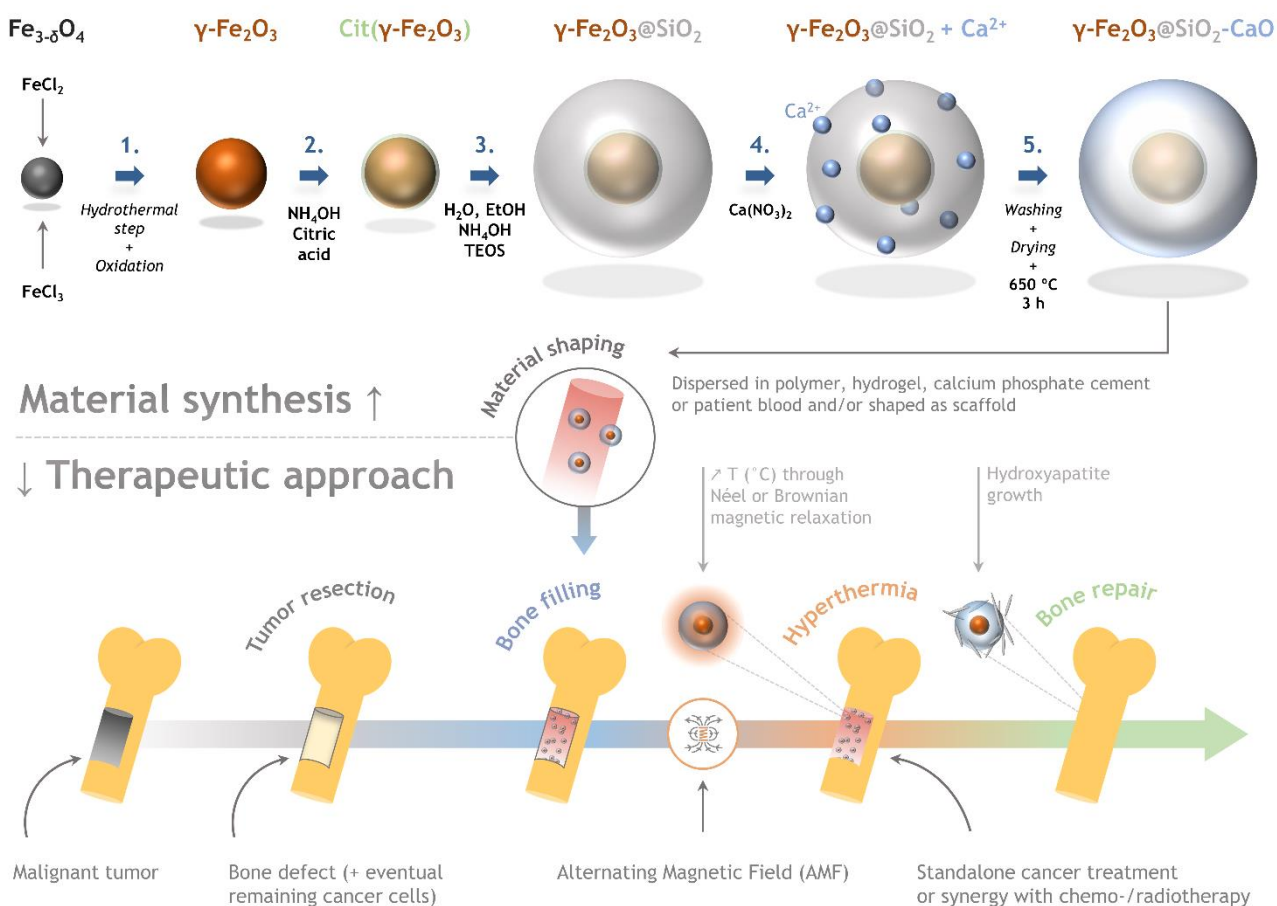


Figure 1. Scheme depicting the different steps for the synthesis of magnetic and bioactive core-shell NPs and the considered therapeutic approach

## Experimental Section

### Materials

Iron (II) chloride tetrahydrate ( $\text{FeCl}_2 \cdot 4\text{H}_2\text{O}$ , 99 %), iron (III) chloride hexahydrate ( $\text{FeCl}_3 \cdot 6\text{H}_2\text{O}$ , 99 %), iron (III) nitrate nonahydrate ( $\text{Fe}(\text{NO}_3)_3 \cdot 9\text{H}_2\text{O}$ , 98 %), nitric acid solution ( $\text{HNO}_3$  65 %), hydrochloric acid solution (HCl 32 %), tetraethyl orthosilicate (TEOS, 99 %), ammonium hydroxide solution ( $\text{NH}_4\text{OH}$  28.0-30 %), and calcium nitrate tetrahydrate ( $\text{Ca}(\text{NO}_3)_2 \cdot 4\text{H}_2\text{O}$ ) were purchased from Sigma-Aldrich. Absolute ethanol (EtOH 99.5 %), acetone and agar powder were obtained from VWR Chemicals. Citric acid monohydrate (99.5 %) was purchased from Labogros. Deionized water was used in all experiments.

### Synthesis of Maghemite ( $\gamma\text{-Fe}_2\text{O}_3$ ) NPs

A colloidal suspension of maghemite NPs was prepared following a protocol previously described by Vichery *et al.*,<sup>42</sup> with some modifications, by coprecipitation of Fe(II) and Fe(III) salts in alkaline medium. First, 11.4 mL of concentrated  $\text{NH}_4\text{OH}$  were quickly poured into 36 mL of a 0.54 M Fe(II) and Fe(III) chlorides solution under vigorous stirring, resulting in the instantaneous formation of a black precipitate of magnetite. The mixture was then transferred in a closed Teflon-lined autoclave for a hydrothermal treatment (150 °C, 7 h) to allow for NPs growth through Ostwald ripening. The flocculate was subsequently washed twice with deionized water, dispersed in 4.9 mL of  $\text{HNO}_3$  (2 M) and kept under stirring for 30 min. After magnetic decantation, the particles were dispersed in an aqueous solution of ferric nitrate (12 mL, 1.5 M) and the mixture was heated up to reflux for 30 min, in order to fully oxidize the magnetite NPs into maghemite. The resulting particles were recovered, washed with acetone before their peptization in an acidic solution (pH = 2) of nitric acid and sonicated. Two centrifugation steps (6460 g / 5 min) were performed in order to reduce the NPs size dispersion. The mass concentration of the resulting ferrofluid was of 31 mg/mL.

Prior to their coating with silica, the iron oxide NPs were functionalized to prevent their agglomeration which could lead to magnetic core clustering inside a single shell. Citric acid is widely used to functionalize the surface of iron oxide NPs and enhance their colloidal stability by electrostatic repulsion.<sup>43</sup> In this purpose, 1 mL of the previously obtained ferrofluid was mixed with 15 mL of a 0.3 M citric acid aqueous solution and kept under stirring for 30 min. Three washing steps with acetone were performed and the citrated particles were peptized in a  $\text{H}_2\text{O}/\text{NH}_4\text{OH}$  (5 mL/2 mL) solution. This resulting citrated ferrofluid will be referred in the following as solution A.

### Synthesis of core-shell ( $\gamma\text{-Fe}_2\text{O}_3@ \text{SiO}_2\text{-CaO}$ ) NPs

Heterostructured NPs were obtained by growing a bioactive glass shell around the maghemite cores *via* a modified Stöber protocol, as previously described by Kesse *et al.*,<sup>30</sup> but with adjusted synthesis parameters. In a typical procedure, two solutions were prepared at room temperature: 6.1 mL of TEOS + 100 mL of EtOH (solution B), and 2 mL of concentrated  $\text{NH}_4\text{OH}$  + 58.5 mL of  $\text{H}_2\text{O}$  + 87.5 mL of EtOH (solution C). Under constant stirring, the solution A (citrated ferrofluid) was quickly poured into solution C. After 10 min of stirring, to ensure proper dispersion, solution B was added to the mixture A+C and the resulting solution was kept under stirring for 3 h. Then, 0.49 g of  $\text{Ca}(\text{NO}_3)_2 \cdot 4\text{H}_2\text{O}$  dissolved in 1 mL of  $\text{H}_2\text{O}$  were poured, and the final suspension was stirred for 21 additional hours. The brown precipitate was collected by centrifugation (6460 g / 10 min) and washed 3 times with deionized water to remove unreacted chemicals. The particles were dried overnight at 60 °C and a final annealing step at 650 °C allowed for the incorporation of  $\text{Ca}^{2+}$  ions into the silica network by diffusion.

### Morphological and structural characterizations

Morphology and size distribution of bare magnetic and heterostructured nanoparticles were observed by transmission electron microscopy (TEM, Hitachi H-7650 operating at 80 kV) on powder samples previously dispersed by sonication in deionized water and deposited on TEM grids. At least 200 particles were analyzed using the ImageJ software to determine particles size distribution and the percentage of single-core heterostructures.

X-ray diffraction (XRD) patterns were recorded in the  $2\theta$  range 20-70 ° with a step of 0.016 ° using a PANalytical X'Pert Pro diffractometer working in Bragg-Brentano configuration with a Cu anode ( $\lambda_{\text{K}\alpha 1} = 1.5406 \text{ \AA}$ ,  $\lambda_{\text{K}\alpha 2} = 1.5444 \text{ \AA}$ ). Diffraction patterns were fitted using the Fullprof suite of programs in order to obtain the sample lattice parameter and the average apparent crystallite size. The procedure is detailed in Supporting Information.

Infrared spectra were acquired by Fourier-transform infrared spectroscopy (FTIR) using a Thermo Scientific Nicolet 5700 spectrometer in transmission mode on KBr pellets. The weight ratio KBr:sample was about 199:1.

The sample composition was determined by inductively coupled plasma-atomic emission spectroscopy (ICP-AES) using a ULTIMA-C spectrometer (HORIBA-Jobin-Yvon). The preparation of sample and reference materials are fully described in a previous article.<sup>30</sup> The analytical wavelengths used for Si, Ca and Fe are  $\lambda = 251.611 \text{ nm}$ ,  $\lambda = 317.933 \text{ nm}$ , and  $\lambda = 259.940 \text{ nm}$  respectively.

Nitrogen adsorption-desorption isotherms were recorded with a Micromeritics Tristar II PLUS sorptometer, and the samples specific surface area were calculated from the Brunauer-Emmett-Teller equation.

Magnetization measurements were performed on powder samples using a Superconducting Quantum Interference Device (SQUID) magnetometer (Quantum Design MPMS3). Magnetization *versus* applied magnetic field curves were recorded at 10 and 300 K and the magnetization values were normalized to the mass of magnetic material, derived from the iron content measured by ICP-AES.

### ***In vitro* bioactivity**

The ability of the heterostructured NPs to form hydroxyapatite in body fluids was assessed *in vitro*. Prior to the assays, simulated body fluid (SBF), a saline aqueous solution mimicking the pH and ion concentrations of human blood plasma, was prepared according to the method described by Kokubo *et al.*<sup>44</sup> The  $\gamma\text{-Fe}_2\text{O}_3\text{@SiO}_2\text{-CaO}$  heterostructures were then soaked in SBF (1 mg/mL) in a plastic beaker and kept in an orbital shaking incubator (N-BIOTEK, NB-205) at 37 °C for 3, 7 and 14 days. To ensure sufficient salt concentrations, the SBF solution was renewed every 7 days. The samples were finally recovered by centrifugation, gently washed twice with deionized water, and dried at 60 °C. The formation of hydroxyapatite crystals was subsequently evidenced by XRD, FTIR and electron microscopy.

### ***In vitro* cytotoxicity tests**

*In vitro* cytotoxicity tests were performed using human mesenchymal stem cells (h-MSCs) by MTT (3-(4,5-dimethylthiazol-2-yl)-2,5-diphenyl tetrazolium bromide) assays following the usual protocol used in the group.<sup>30</sup> This choice of cell type was based on the desire to be as close as possible to the clinical application of the material. In a typical procedure, metaphysic cancellous bone tissues were collected during hip arthroplasty surgical procedures performed on patients who gave their consent beforehand for the use of their bones for research purposes. Then, they underwent multiple steps of treatment and culture, in order to collect the h-MSCs, as fully detailed by Jacobs *et al.*<sup>45</sup>

Prior to the cytotoxicity tests, the heterostructured NPs were sterilized by keeping them in an oven at 180 °C for 2 h. Then, h-MSCs cultured in minimum essential medium (MEM) were seeded in a 24-well plate, exposed to the nanopowders with a concentration of 1 mg/mL, and incubated at 37 °C for 3 or 7 days. MEM-cultured h-MSCs without powder were used as a control. After incubation, the mitochondrial activity of the cells was evaluated using MTT. The MTT salt being reduced to purple formazan crystals by metabolically active cells, after dissolution, samples cytotoxicity can be quantified by spectrophotometry (TECAN) through the measurement of the solution optical density at 570 and 690 nm. The darker the solution, the greater the number of viable, metabolically active, cells. Mann-Whitney statistical tests were performed on the data sets (with  $n = 3$  replicates) using Past software, to evaluate statistical significance.

## Magnetic hyperthermia study

**Specific loss power measurements.** The specific loss power (SLP), or specific absorption rate (SAR), was measured by calorimetry using a magnetic hyperthermia apparatus from NanoScale Biomagnetics (D5 Series, Driver G2 Multi-mode 1500 W). The nanopowders were thoroughly dispersed in water through sonication (NPs concentration of 68.1 mg/mL), leading to an iron concentration of 0.8 mg<sub>Fe</sub>/mL, based on the ICP-AES measurements. An adapted glass vial was filled with 1 mL of this suspension and subjected to an alternating magnetic field (AMF) while recording the temperature evolution with a fiber-optic temperature probe. Temperature profiles *versus* AMF application time were recorded using the associated MaNiaC software. For some measurements, the particles were immobilized in agar. The samples were prepared following a similar protocol: the NPs were first dispersed in water with a concentration of 0.6 mg<sub>Fe</sub>/mL, and then agar powder was added in the dispersion (1 wt % agar/water).

Hyperthermia measurements were performed under different AMF frequencies ( $f = 157.1, 303.7, 383.1, 492.9, 636.8$  and  $768.5$  kHz), and amplitudes ( $H_0 = 11.9, 15.9$  and  $23.9$  kA/m). Each measurement lasted 3 min and was performed 3 times.

The SLP values were extracted from the temperature profiles by the initial slope method, using a 2<sup>nd</sup> order polynomial function to fit the plots and to determine  $(\Delta T/\Delta t)_{t=0}$ . Indeed, the increase in temperature at the beginning of the measurement is considered as characteristic of an adiabatic system. SLP values are finally obtained using the following expression:

$$SLP = \frac{m_{H_2O}C_{H_2O} + m_{NPs}C_{NPs}}{m_{Fe}} \left( \frac{\Delta T}{\Delta t} \right)_{t=0} \quad (1)$$

where SLP is expressed per unit mass of iron ( $W/g_{Fe}$ ),  $m$  and  $C$  are the mass and specific heat capacity of dispersion medium and nanoparticles ( $C_{H_2O} = 4.18 \text{ J}\cdot\text{g}^{-1}\cdot\text{K}^{-1}$  and  $C_{NPs} = \%_{wt}(\gamma\text{-Fe}_2\text{O}_3) \times C_{\gamma\text{-Fe}_2\text{O}_3} + \%_{wt}(\text{SiO}_2\text{-CaO}) \times C_{\text{SiO}_2\text{-CaO}}$ , with  $C_{\gamma\text{-Fe}_2\text{O}_3} = 0.65 \text{ J}\cdot\text{g}^{-1}\cdot\text{K}^{-1}$  and  $C_{\text{SiO}_2\text{-CaO}} \approx C_{\text{SiO}_2} = 0.92 \text{ J}\cdot\text{g}^{-1}\cdot\text{K}^{-1}$ ),<sup>46</sup>  $m_{Fe}$  the mass of iron inside the sample as determined by AES and  $(\Delta T/\Delta t)_{t=0}$  the initial slope.

**Theory of heat generation for SLP prediction.** In superparamagnetic (SPM) materials, heat generation mainly occurs through relaxation mechanisms because of their low coercivity and remanence, leading to negligible hysteresis losses. It is well known that in response to an alternating magnetic field, the magnetization of SPM particles can relax and cause thermal losses either through two mechanisms:<sup>16,47</sup>

- Néel relaxation, where the magnetization rotates within the particle and is hindered by the anisotropy energy that tends to orientate it along the easy axis. If we consider the anisotropy constant  $K_{eff}$ , the magnetic volume  $V$  and the Boltzmann constant  $k_B$ , the Néel relaxation time  $\tau_N$  is given by:

$$\tau_N = \tau_0 \cdot \exp\left(\frac{K_{eff}V}{k_B T}\right) \quad (2)$$

- Brownian relaxation, where the rotation of the particle itself, of hydrodynamic volume  $V_H$ , is hindered by the viscosity  $\eta$  of the surrounding medium, leading to a brownian relaxation time  $\tau_B$  defined as:

$$\tau_B = \frac{3\eta V_H}{k_B T} \quad (3)$$

One can define the effective relaxation time  $\tau_R$  that depends on Néel and Brownian relaxation times as:

$$\tau_R^{-1} = \tau_N^{-1} + \tau_B^{-1} \quad (4)$$

The shortest relaxation time determines which mechanism is dominant, but in most of the cases, the effective relaxation time is a combination of both. A common way to predict thermal losses and thus the SLP for particles depending on these two relaxation mechanisms is the linear response theory (LRT).<sup>16,47</sup> In the framework of the linear response model, an expression of the power dissipation  $P$  (in  $W/m^3$ ) has been proposed by Rosensweig as:<sup>48</sup>

$$P = \mu_0 \pi \chi''(f) H_0^2 f \quad (5)$$

where  $\mu_0$  is the permeability of free space,  $\chi''$  the loss component of the magnetic susceptibility of the material and  $f$  and  $H_0$  respectively the AMF frequency and amplitude.  $\chi''$  is frequency-dependent and can be expressed as:

$$\chi''(f) = \frac{2\pi f \tau_R}{1 + (2\pi f \tau_R)^2} \chi_0 \quad (6)$$

where  $\chi_0$  is a constant depending on the SPM particles intrinsic properties: the saturation magnetization ( $M_s$ ), and the volume of particle ( $V$ ). Given the expression of SLP =  $P/\rho$  (in W/g), with  $\rho$  the mass density of magnetic material, substituting the expression of  $\chi''(f)$  in equation 2 yields:

$$SLP = \frac{\mu_0 \pi \chi_0 H_0^2 f}{\rho} \frac{2\pi f \tau_R}{1 + (2\pi f \tau_R)^2} \quad (7)$$

## Results and Discussion

### Nanoparticles morphological and structural characterizations

The multifunctional bioactive and magnetic heterostructures were obtained through a multi-step synthesis previously studied in our research team.<sup>30</sup> To obtain such heterostructures, it was proposed to grow a bioactive glass shell around previously formed iron oxide NPs. One major advantage of this approach over one-pot routes is the ability to finely control the size and crystallinity of the bare magnetic cores and therefore to study their properties prior to BG encapsulation, providing leverage to obtain optimal magnetic properties for hyperthermia.

In a first step, maghemite NPs were synthesized through coprecipitation of Fe(II) and Fe(III) salts in alkaline medium. Then, a hydrothermal treatment was carried out, to tune the particle size *via* Ostwald ripening. Selected temperature and step duration, which are the main factors influencing the final NPs size, allowed to obtain spheroidal, slightly faceted NPs (Fig. 2A).<sup>49</sup> In a last step, the NPs were fully oxidized into maghemite. By fitting the size histogram with a log-normal function, the magnetic NPs mean size was determined as  $16 \pm 3$  nm, showing a moderate size dispersity of 21% (Fig. 2B).

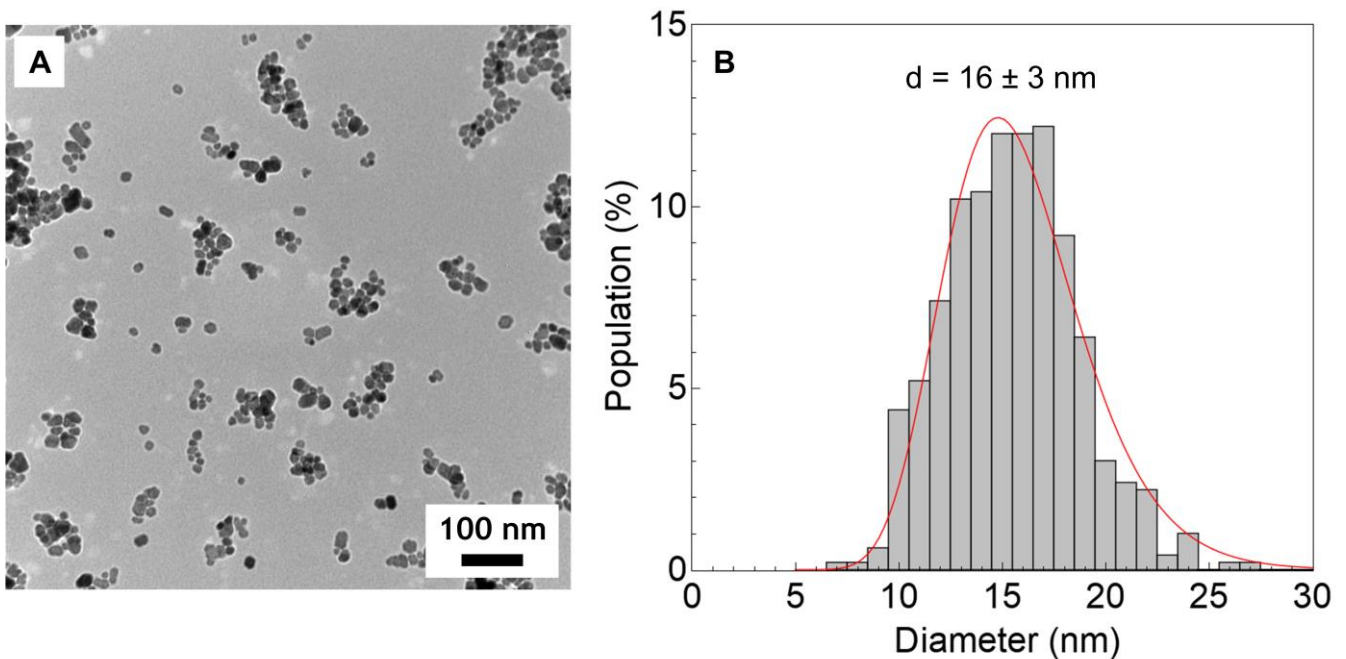


Figure 2. Representative TEM image (original magnification  $\times 150000$ ) (A) and size histogram fitted with a log-normal function (B) of the magnetic NPs

The X-ray diffraction pattern of the magnetic NPs shows the characteristic Bragg peaks of spinel ferrites (see Fig. 3), confirming the presence of either magnetite ( $\text{Fe}_3\text{O}_4$ ) or maghemite ( $\gamma\text{-Fe}_2\text{O}_3$ ). The determination of the lattice parameter  $a$  by full-pattern matching is a method that allows to accurately discriminate between the two phases as  $a = 8.396 \text{ \AA}$  for magnetite (JCPDS 19-0629) and  $a = 8.352 \text{ \AA}$  for maghemite (JCPDS 39-1346). Here, the refinement led to a lattice parameter value of  $8.358 \pm 0.001 \text{ \AA}$ , which is in agreement with the theoretical value of maghemite (see Figure S1 in Supporting Information). An average apparent crystallite size of about  $15 \pm 2 \text{ nm}$  was obtained from the full pattern matching refinement. This value is consistent with the mean particle size derived from the TEM images, thus indicating that the particles are monocrystalline.

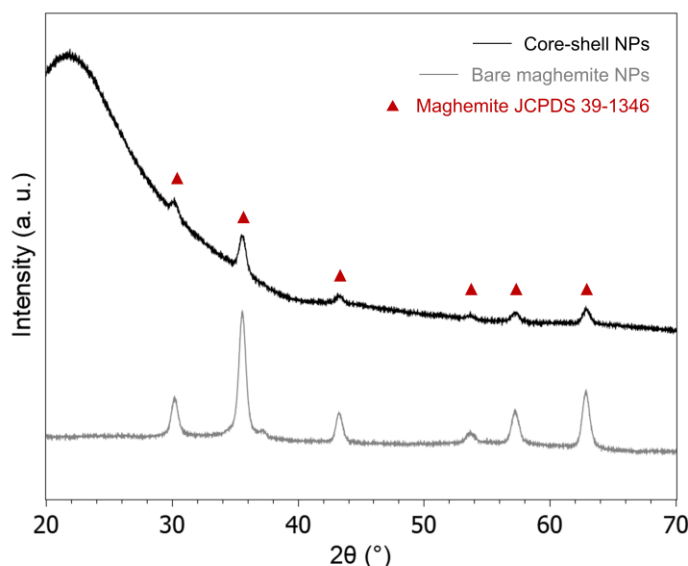


Figure 3. Diffraction patterns of the maghemite (gray, bottom) and the heterostructured NPs (black, top)

Prior to the bioactive shell growth, the maghemite NPs were citrated to increase their colloidal stability in the basic reaction medium and to avoid magnetic core aggregation before or during the encapsulation process. Indeed, after citration, the point of zero charge of maghemite NPs is shifted to lower values of pH thanks to the deprotonation of up to three carboxyl groups ( $\text{pK}_a$  of 3.13, 4.76 and 6.40 respectively).<sup>50</sup> The citrated NPs thus present a highly negatively charged surface in a wide range of pH that allows electrostatic repulsion. Moreover, the high nucleophilic surface of citrated iron oxide NPs indulges preferential growth sites for the silica shell.<sup>51</sup>

The growth of a bioactive glass shell around the magnetic cores was based on a modified Stöber method. First, the silica shell was made by a classical sol-gel route in alkaline medium. Calcium nitrate was added 3 h later and non-reacted species were removed with a washing step. A thermal treatment allowed for calcium diffusion inside the silica matrix. This multi-step approach provided a good control on the size, dispersity, morphology and aggregation of the final heterostructured NPs. Indeed, calcium nitrate is known to disturb Stöber silica growth if added early in the reaction medium, when silica primary particles are small and highly reactive, and leads to irregular shape, inhomogeneity in size and/or aggregation.<sup>52,53</sup> Despite a decrease in incorporated calcium quantity, it has been shown that a  $\text{Ca}^{2+}$  addition time of 1 to 3 hours after the beginning of the sol-gel reaction led to monodisperse and non-agglomerated BG NPs.<sup>52</sup>

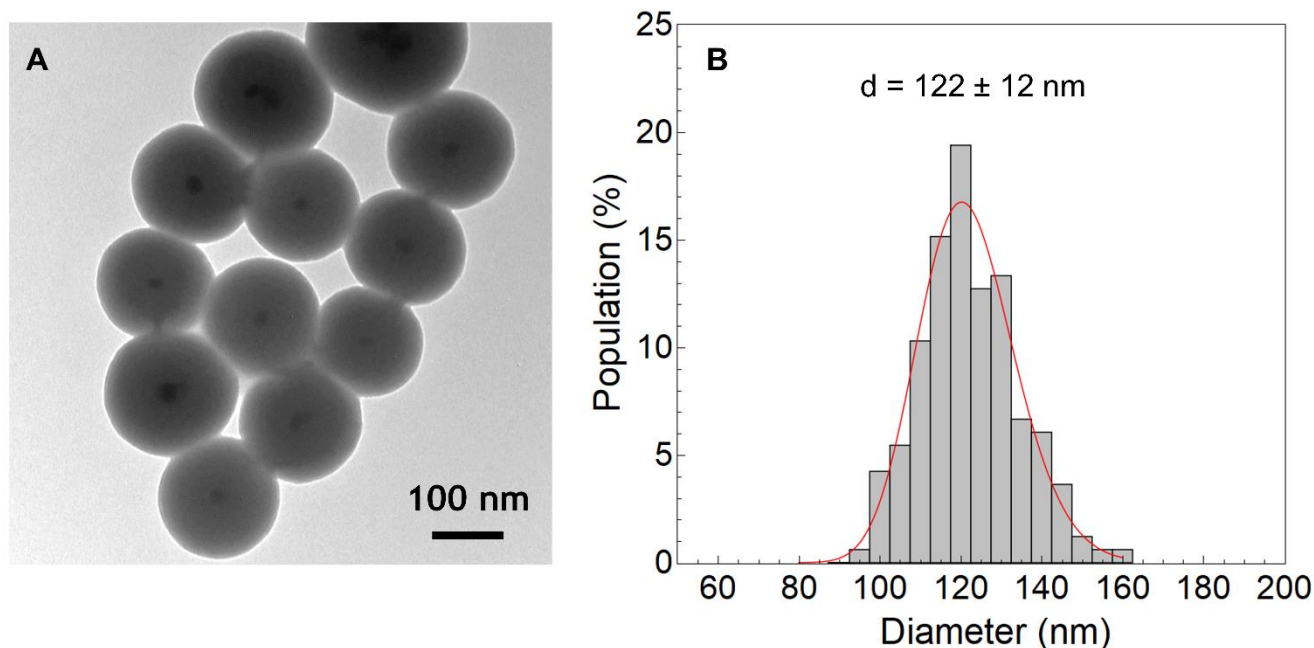


Figure 4. TEM image (original magnification  $\times 200000$ ) (A) and size histogram fitted by a log-normal function (B) of the  $\gamma\text{-Fe}_2\text{O}_3\text{@SiO}_2\text{-CaO}$  heterostructures

TEM images show an effective growth of silica around the magnetic NPs, which can be deduced from the difference of contrast between the iron oxide cores and the glass shells (Fig. 4A). These core-shell heterostructures are mainly single-core ( $\sim 53\%$ , see Fig. S2 in Supporting Information). Also, all the magnetic NPs were encapsulated, and no homogeneous growth of silica (pure BG NPs) was observed. This could be explained by the relatively good colloidal stability of the magnetic NPs in the reaction medium (provided by the citrate functionalization and the control on magnetic NPs size and concentration). Furthermore, heterostructured NPs are non-aggregated, spherical, and quite monodispersed in size ( $122 \pm 12$  nm, Fig. 4B).

**Table 1.** Composition of the heterostructured NPs determined by ICP-AES. Relative analytical error on mass fraction is about 1 % and relative error on molar fraction results is about 2 %.

	<b>SiO<sub>2</sub></b>	<b>CaO</b>	<b>Fe<sub>2</sub>O<sub>3</sub></b>
Mass fraction (%)	91.92	6.37	1.71
Molar fraction (%)	92.48	6.87	0.65

Elemental analysis by ICP-AES results (Table 1) show that calcium was effectively incorporated in the glass network and confirm the presence of iron in the composite. The XRD pattern of the heterostructures shows diffuse scattering attributed to the glass network and the unchanged Bragg peaks of maghemite (Fig. 3). The glass encapsulating the magnetic cores thus preserved the maghemite NPs from any phase transition to hematite ( $\alpha\text{-Fe}_2\text{O}_3$ ) during the  $650^\circ\text{C}$  thermal treatment,<sup>42</sup> and no crystalline impurities such as calcium carbonate and/or silicates that could be caused by the calcium salt addition are observed.

$\text{N}_2$  sorption measurements are useful to complement these results. Besides showing an adsorption isotherm typical of a non-porous nanomaterial (Fig. S3 in Supporting Information), a specific surface area ( $S_{\text{BET}}$ ) of about  $27 \text{ m}^2/\text{g}$  was obtained for the heterostructured NPs. Considering spherical particles, the theoretical mean diameter derived from  $S_{\text{BET}}$  would range from 100 to 120 nm, confirming the non-agglomerated state of the NPs (see detailed calculation in Supporting Information).

## Magnetic characterizations

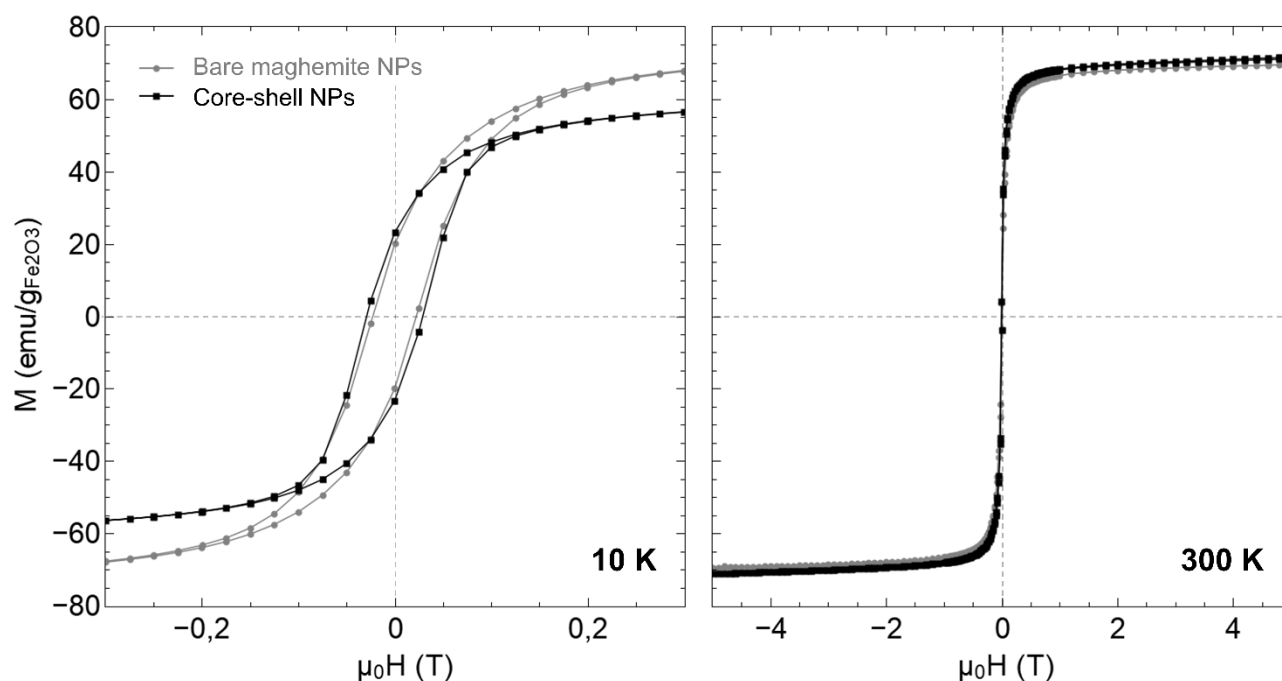


Figure 5.  $M(H)$  magnetization curves of maghemite (gray, circles) and heterostructured (black, squares) NPs at 10 K and 300 K

The magnetization *versus* applied magnetic field curves for bare maghemite and heterostructured NPs were recorded at 10 and 300 K and normalized to the mass of iron oxide in the samples, based on ICP-AES results. As shown in Fig. 5, for both samples, the curve at 10 K reveals a small coercivity ( $\sim 25$  mT) and the one at 300 K is typical of a superparamagnetic material with no hysteresis.<sup>54</sup> The absence of coercivity and remanence at room temperature is ideal for healthcare applications, as the magnetization is suppressed as soon as the magnetic field is stopped, thus preventing particle agglomeration. One can see in Fig. 5 that the magnetic properties were not significantly altered by the encapsulation of the magnetic cores and that the high saturation magnetization value at room temperature ( $M_s = 70 \pm 1$  and  $72 \pm 1$  emu/g<sub>Fe<sub>2</sub>O<sub>3</sub></sub> for bare and core-shell NPs respectively) is close to the one of bulk maghemite (74 emu/g).<sup>55</sup> For the heterostructures, the saturation magnetization value at 300K, normalized to the total sample mass, is of 1.22 emu/g. It is an interesting value regarding the low iron content ( $< 1$  %mol), especially compared to  $M_s$  values from similar systems presented in the literature, synthesized through one-pot synthesis. Indeed, due to the poor control of the magnetic NPs nucleation and growth, in the work of Li *et al.* the  $M_s$  value reaches only as high as 3.57 emu/g despite a more than 10 times higher iron content,<sup>56</sup> and in other studies,  $M_s$  values remain below 1 emu/g with a similar iron content.<sup>57,58</sup> On the other hand, while using preformed iron oxide NPs, other authors obtained higher  $M_s$  values depending on the SPIONs content, from 1.58 to 3.48 emu/g for SPIONs-loaded BG scaffold,<sup>26</sup> 14.16 emu/g,<sup>59</sup> and up to 17.88 emu/g,<sup>60</sup> for encapsulated SPIONs in BG. In their review on bioactive glass in cancer therapy, Sharifi *et al.* reached the same conclusion while comparing magnetic responsive mesoporous BGs.<sup>61</sup> Here, the heterostructures  $M_s$  value referred to the total sample mass is strongly reduced due to the large shell thickness ( $> 50$  nm) and thus high relative amount of BG in the sample. It could easily be increased by reducing the shell thickness or increasing SPIONs loading.

## Bioactivity and cytotoxicity results

***In vitro* bioactivity.** The  $\gamma$ -Fe<sub>2</sub>O<sub>3</sub>@SiO<sub>2</sub>-CaO heterostructures presented in this study are intended to be used as a bone substitute after bone tumor resection. For such application, the SiO<sub>2</sub>-CaO glass shell is expected to interact with the body when implanted to ensure a more efficient bone repair. The bioactivity of BG is usually characterized by the ability to promote bone repair *via* surface dissolution phenomena and crystallization of

hydroxyapatite (HAp) at its surface, when immersed in a biological medium.<sup>20</sup> This nanocrystalline carbonated hydroxyapatite formed is by nature very close to biological apatite, the major inorganic component of natural bones, which allows enhancing the bonding between the graft and bone tissues. Furthermore, calcium and silicon ionic dissolution products are known to play key roles in bones metabolism processes, *i.e.* they are essential for the formation and calcification of bone tissues, stimulate collagen formation, favor osteoblasts proliferation and differentiation and extracellular matrix mineralization.<sup>23</sup>

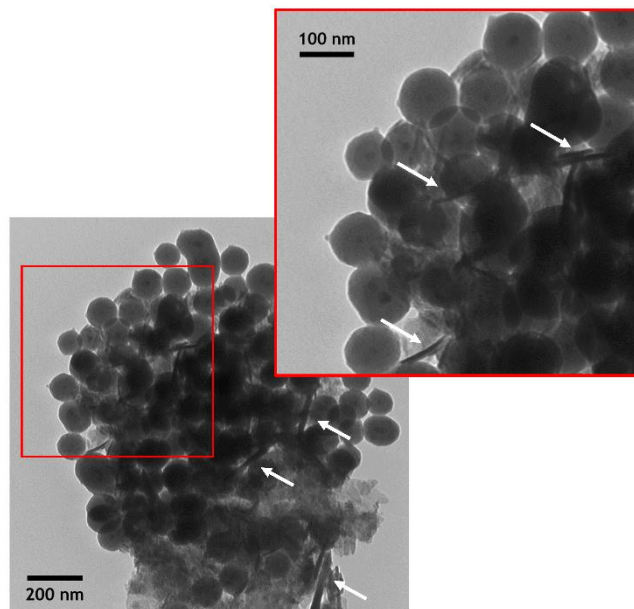


Figure 6. TEM image of the bioactive and magnetic core-shell NPs after 14 days of immersion in SBF. Needle-like nanocrystals are pointed by white arrows

It is commonly accepted that monitoring hydroxyapatite crystallization in SBF is an efficient way to predict a material's bioactivity, as its formation will also be expected in the living body.<sup>44</sup> In this study, the core-shell NPs were soaked in SBF for up to 14 days. TEM images (Fig. 6) exhibit needle-like nanocrystals surrounding the heterostructured NPs after 14 days of immersion in SBF, and their nature (HAp) was confirmed by XRD and FTIR spectroscopy.

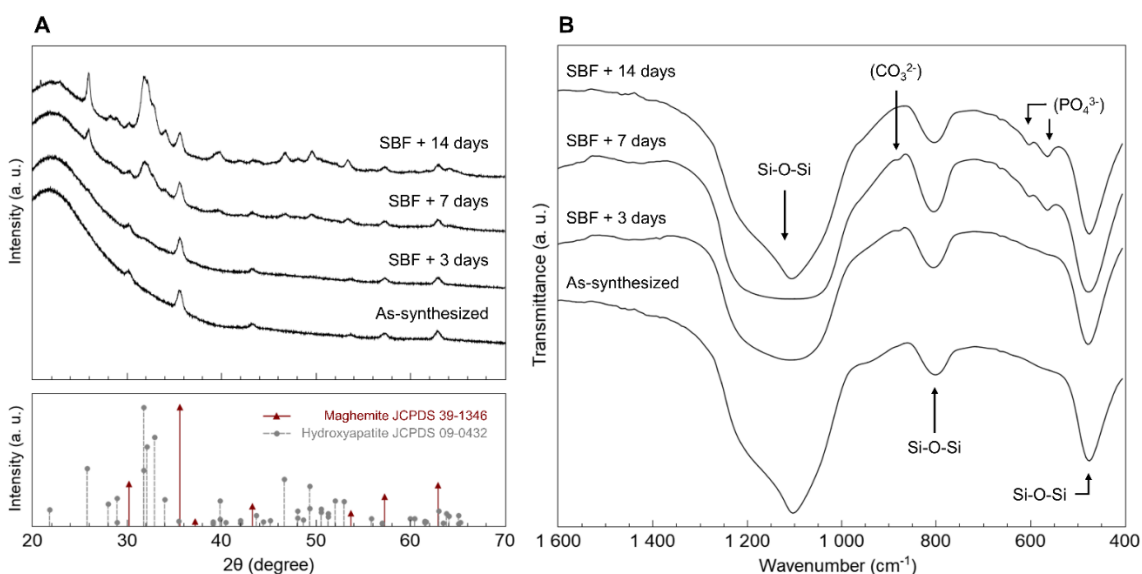


Figure 7. XRD patterns (A) and FTIR spectra normalized to the Si-O-Si band at 475 cm<sup>-1</sup> (B) of heterostructured NPs before and after up to 14 days of immersion in SBF

The Fig. 7A shows the XRD patterns of the heterostructures after immersion in SBF. One can see the apparition of Bragg peaks characteristic of HAp (JCPDS 09-0432) after 7 days of immersion in SBF, meaning that HAp crystals started to grow between 3 and 7 days. Such a fast apatite formation kinetics for a binary glass shell with a low calcium content can be explained by the bioactive glass intrinsic textural properties, specifically the higher specific surface area thanks to the small particle size compared to melt-quenched BG particles.<sup>21,62</sup>

This kinetic was confirmed by FTIR, as the spectrum after 7 days of immersion in SBF exhibits new bands at 564 and 604  $\text{cm}^{-1}$ , corresponding to the O-P-O bending vibrations of HAp phosphate groups.<sup>63</sup> The band at 879  $\text{cm}^{-1}$  can be attributed to the O-C-O bending vibration of carbonate groups,<sup>63</sup> indicating the formation of carbonated HAp. These results prove that the heterostructures are reactive in biological medium and could promote bone regeneration.

***In vitro* cytotoxicity.** A proof of the cytocompatibility is a mandatory step for any material intended to be used in contact with a living body. An *in vitro* viability test is a good first approach to assess the cytotoxicity of a material. For this purpose, the viability of h-MSCs was assessed by MTT assays in the presence of the heterostructured NPs after 3 and 7 days of incubation. As shown in Fig. 8 there is no reduction in the metabolic activity, which does not change significantly after 3 or 7 days, as  $p > 0.05$  compared to the control h-MSCs incubated without the NPs. These core-shell NPs can thus be considered as nontoxic.

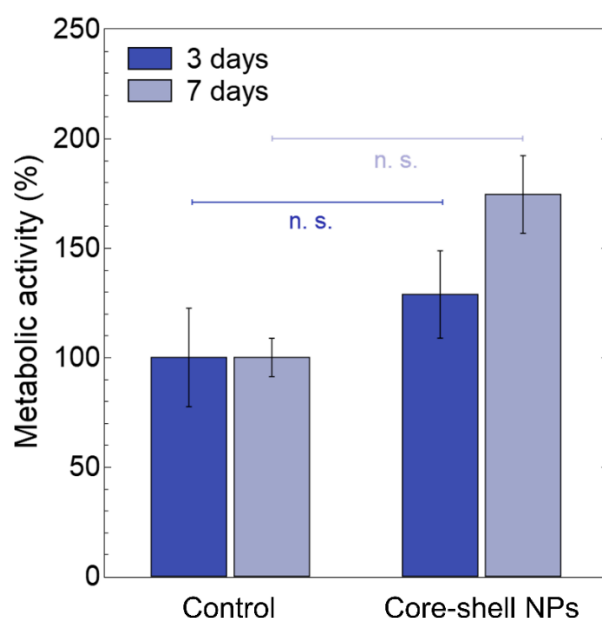


Figure 8. Metabolic activity (MTT assays) of h-MSCs alone (control) or in the presence of heterostructured NPs, after 3 or 7 days of incubation. Error bars represent the standard mean error from  $n = 3$  replicates. n.s.: not significant, corresponds to  $p > 0.05$

### Magnetic hyperthermia study

The key application of these multifunctional NPs is the use of magnetic hyperthermia (MH) to treat residual or resurgent cancer cells after a bone tumor resection. The local temperature rise at the implantation site could be used to selectively destroy cancer cells or to enhance existing treatments such as chemotherapy or radiotherapy.

The heat dissipated by a material upon stimulation – an AMF in the case of MH – is called the specific loss power. The SLP value is usually normalized per gram of magnetic material and depends on the material intrinsic properties and the magnetic field parameters. In the literature, the SLP is estimated using a wide range of AMF parameters,<sup>26,30,64–68</sup> which highlights two issues.

First, the importance to take into account the clinical relevance for the choice of AMF parameters if the material is intended to be designed for medical applications. One commonly admitted criterion for local hyperthermia is the one proposed by Hergt and Dutz, where the product of field amplitude and frequency

must satisfy  $H_0 \times f < 5 \cdot 10^9 \text{ A m}^{-1} \text{ s}^{-1}$ .<sup>69</sup> Commercial hyperthermia clinical equipment usually operates within this range.<sup>70</sup> When the product  $H_0 \times f$  is above this criterion, the AMF can cause unwanted heating of healthy tissues due to the generation of eddy currents and the patient can experience discomfort.

Second, normalization or standardization is highly important in order to be able to compare the heating power of the materials presented in different studies. Indeed, the measurements can be performed using a wide range of field parameters and not necessarily considering the above-mentioned clinical criterion. The intrinsic loss power (ILP), defined as:

$$\text{ILP} = \frac{\text{SLP}}{f H_0^2} \quad (8)$$

is a useful tool to normalize and compare samples measured with different AMF parameters. However, its definition implies that the SLP is linearly dependent on the frequency, an approximation not always satisfied for magnetic NPs dispersed in a fluid because of the strong dependence of the loss component of the magnetic susceptibility  $\chi''$  (equation 6) on frequency in the hyperthermia range.<sup>48</sup> This non-linear behavior was also reported experimentally by different authors.<sup>65,71</sup>

Consequently, with the aim i) to compare the performance of the heterostructured particles presented in this work with the literature, ii) to study the SLP behavior as a function of the AMF parameters, and iii) to define the best amplitude/frequency set with respect to the Hergt and Dutz criterion, calorimetric measurements were performed under different AMF amplitudes ranging from 11.9 to 23.9 kA/m and frequencies from 157.1 to 768.5 kHz. Prior to the measurements of heterostructures dispersed in water, the temperature of pure water was recorded under an applied AMF with the maximal values of frequency and amplitude. As presented in Fig. S4 in Supporting Information, after 3 min, a temperature rise of only 0.3 °C was observed. Regarding the heterostructured NPs dispersed in water, six AMF amplitude-frequency pairs met the clinical criterion, and their heating curves are presented in Fig. 9. After 3 min of field application, a temperature rise of about 4 °C starting from room temperature was reported using a field amplitude of 23.9 kA/m and a frequency of 157.1 kHz. It is noteworthy that a greater temperature increase can be achieved as the curves did not saturate in this set of experiments. The measurement system being pseudo-adiabatic, the temperature increases with time, but not strictly linearly due to heat losses. The temperature *versus* time profiles were thus fitted and the SLP was extracted using the initial slope method for each  $H_0 \times f$  pair. The fitted heating rates  $(\Delta T / \Delta t)_{t=0}$  and details of SLP calculation can be found in the table S1 in Supporting Information.

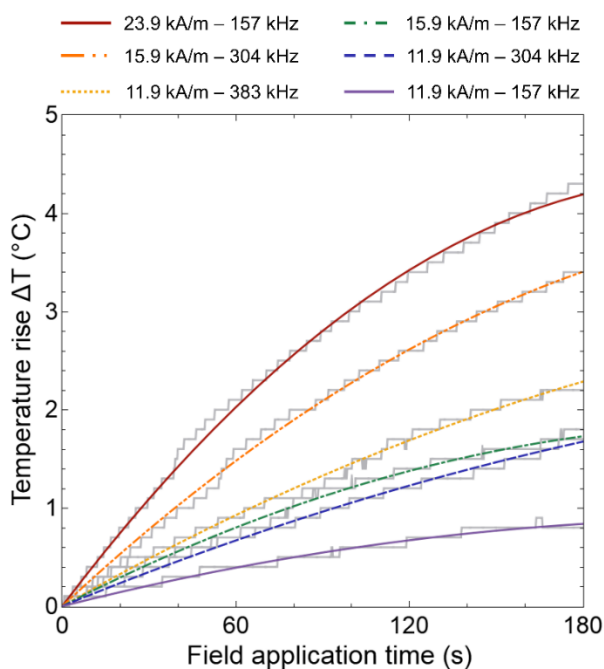


Figure 9. Temperature profiles and fitted polynomial curves as a function of time under different AMF parameters ( $H_0$ - $f$ ) of clinical relevance

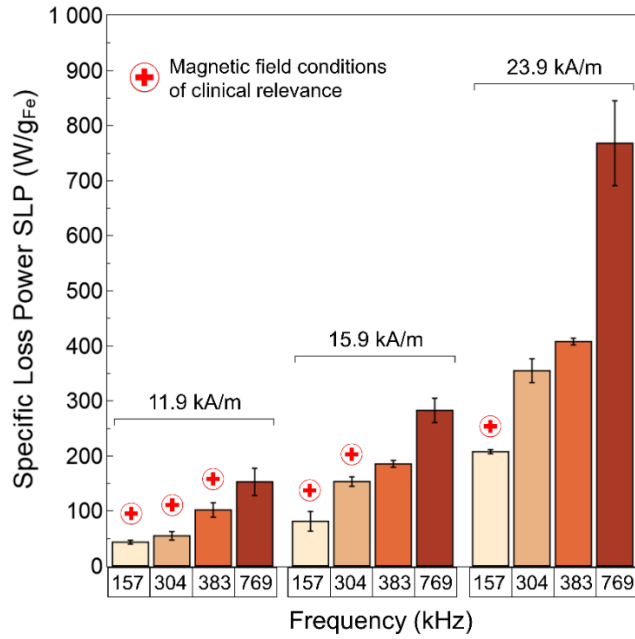


Figure 10. Specific loss power values for measurements using various AMF frequencies (157 to 769 kHz) and amplitudes (11.9 to 23.9 kA/m). Clinically relevant conditions are enlightened

Fig. 10 presents the range of SLP values achieved for the hyperthermia measurements with multiple sets of AMF parameters. It also highlights the SLP values obtained under clinically relevant AMF parameters. Regarding the heating profiles and SLP values, it appears to be more beneficial to increase the field amplitude rather than its frequency. This is consistent with previous experimental finding<sup>66,72</sup> as well as with the theory. In Rosensweig's model, the SLP value depends on the applied magnetic field amplitude  $H_0$  and frequency  $f$ , and on intrinsic material properties such as  $\rho$ ,  $\chi_0$  and  $\tau_R$ . According to the equation 7, the heating power increases quadratically with the field amplitude ( $SLP \propto H_0^2$ ) and depends on the frequency as  $SLP \propto A \times Bf^2 / (1+(Bf)^2)$  with  $A = (\mu_0\pi\chi_0/\rho)H_0^2$  and  $B = 2\pi\tau_R$ .

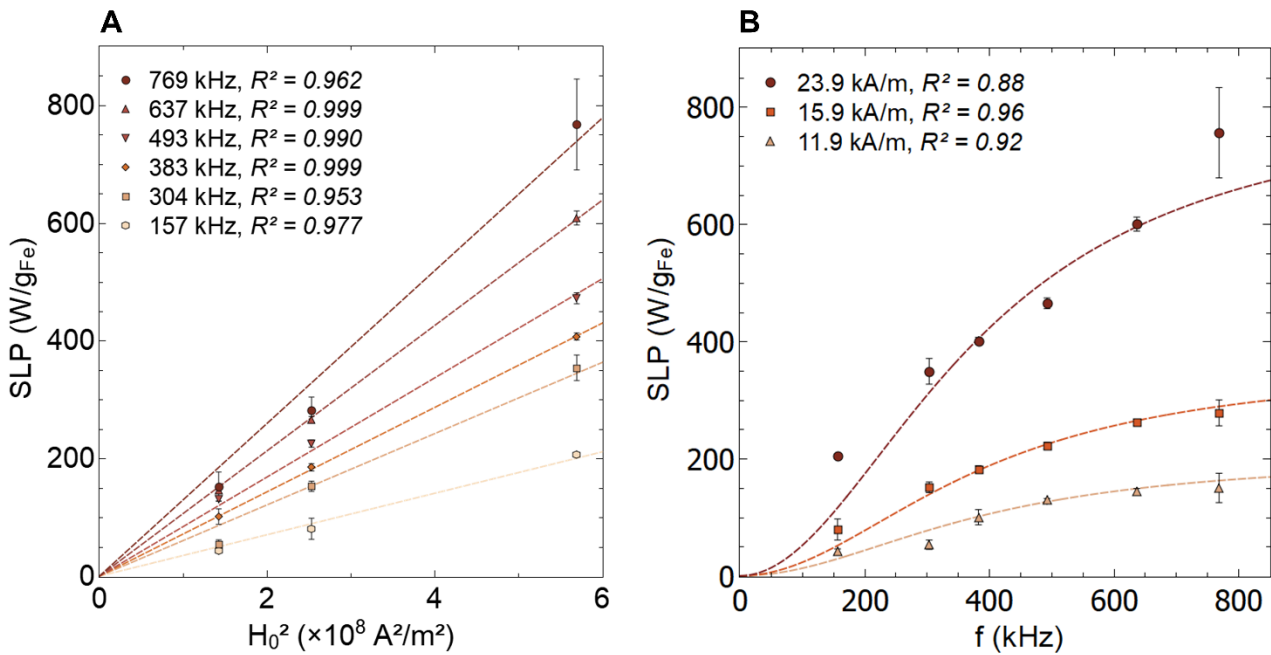


Figure 11. Evolution of measured specific loss power with the square of AMF amplitude (A) and with field frequency (B) along with the fit with LRT model. Adjusted  $R^2$  values are indicated for goodness of fit

As it can be seen in Fig. 11A, the experimental SLP values in this study indeed evolve linearly with  $H_0^2$ , therefore, it can be stated that the SLP behavior follows the LRT model.<sup>73-75</sup> The evolution of the measured SLP values *versus* frequency can thus be fitted using the following equation, derived from the equation 7:

$$\text{SLP} = aH_0^2 \cdot \frac{2\pi f^2 \tau_R}{1+(2\pi f \tau_R)^2} \quad (9)$$

where  $a = \mu_0 \pi \chi_0 / \rho$  and  $\tau_R$  are constants that are not affected by the AMF parameters and only depend on the material or the surrounding medium intrinsic properties. The values of  $a$  and  $\tau_R$  for a given field amplitude  $H_0$  can thus be directly obtained from the fit of experimental SLP as a function of frequency, using equation 9. All other things being equal,  $a$  and  $\tau_R$  should not depend on  $H_0$ , hence  $a$  and  $\tau_R$  values were first varied and a set of values was chosen to fit all experimental curves for the 3 different amplitudes. The procedure that led to the determination of the best set of parameters to fit the 3 curves is detailed in Supporting Information. The fits using the equation 9 with  $a = 2.681 \times 10^{-9} \text{ J} \cdot \text{kg}^{-1} \cdot \text{A}^{-2} \cdot \text{m}^2$  and  $\tau_R = 4.369 \times 10^{-7} \text{ s}$  are presented in dashed lines in Fig. 11B. The determined  $\tau_R$  agrees well with an expected relaxation time value of about  $10^{-7}$  to  $10^{-6}$  s for  $\gamma\text{-Fe}_2\text{O}_3$  NPs of about 16 nm diameter.<sup>71,76</sup>

According to the equation 7, the SLP varies with the square of frequency when  $2\pi f \tau_R < 1$  and saturates when  $2\pi f \tau_R \gg 1$ . Here, the frequency value respecting the equation  $2\pi f \tau_R = 1$  is about 364 kHz. This experimental result, consistent with the Rosensweig predictions, confirms the advantage of working with a lower field frequency associated with a field amplitude as high as possible when the goal is to respect  $H_0 \times f < 5 \cdot 10^9 \text{ A} \cdot \text{m}^{-1} \cdot \text{s}^{-1}$  to be in clinically relevant conditions. This behavior is clearly shown in Fig. 10, where the highest clinical SLP value corresponds to the highest amplitude coupled with the lowest frequency.

It is interesting to note that the intrinsic loss power (ILP) values can be directly extracted from the slopes in Fig. 11A (dashed lines) as  $\text{SLP} = \text{ILP} \times f \times H_0^2$  by definition. ILP values still depend on AMF parameters because of the frequency dependence of the magnetic susceptibility as evidenced in equations 7 and 8 (Rosenweig model). This behavior is depicted in Fig. 12 (black dots), where the ILP values calculated for each field conditions using the equation 8 are also presented, for the sake of comparison.

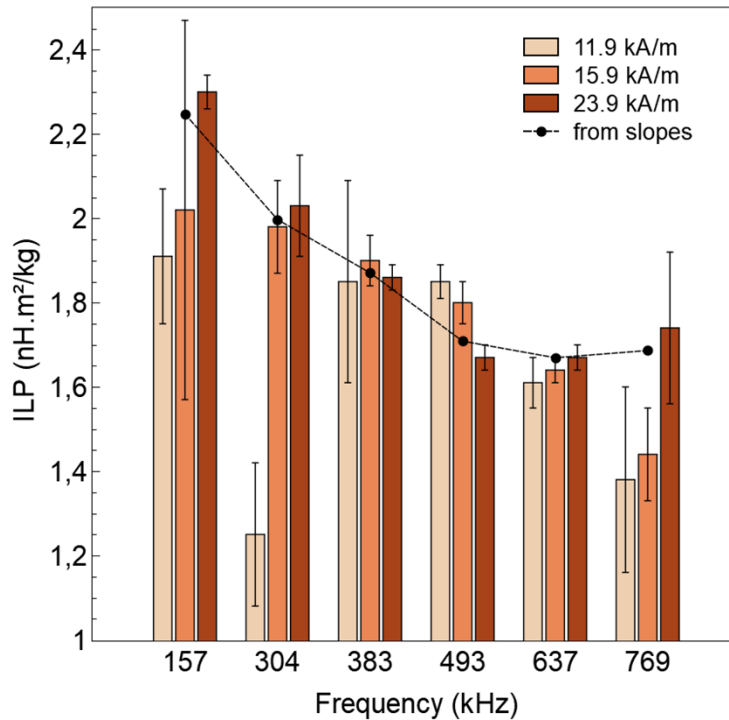


Figure 12. Evolution of intrinsic loss power (ILP) with field frequency. Black circles: values obtained from the fits of the SLP versus  $H_0^2$  curves (the dashed line is a guide to the eye). Vertical bars: values calculated for each set of AMF parameters, from the equation  $\text{ILP} = \text{SLP}/f \cdot H_0^2$

For the calculated ILP values, even if no global trend is observed, variations with field amplitude are noticeable. The advantage of the ILP values extracted from the SLP *versus*  $H_0^2$  curves is that it allows to obtain a single value for any  $H_0$ . This determination method would be of great interest to more effectively and reliably compare the ILP values of different samples from the literature (for a fixed field frequency). In the frequency spectrum investigated here, the ILP values for the  $\gamma\text{-Fe}_2\text{O}_3\text{@SiO}_2\text{-CaO}$  heterostructures range from 1.67 to 2.25  $\text{nH}\cdot\text{m}^2/\text{kg}_{\text{Fe}}$ . These values are really close to the ones of similar core-shell NPs for medical hyperthermia applications using SPIONs found in the literature, as shown in the Table 2. Modest ILP values for some other nanosystems such as the ones in the studies of Kesse *et al.*<sup>30</sup> and Guisasola *et al.*<sup>67</sup> could be explained by the SPIONs ultrasmall size, leading to lower  $M_s$  values due to an enhanced contribution of disordered surface spins (spin canting). Some other works on magnetic and bioactive systems (scaffolds) did not report any SLP value but showed promising results: a temperature rise of 17 °C within 5 min (10 mg of material under  $H_0 = 14.4$  kA/m and  $f = 409$  kHz),<sup>26</sup> and for another study, a  $\Delta T$  of 8.25 °C after 25 min (200 mg of material in 3 mL of water, with  $H_0 = 1.47$  kA/m and  $f = 232$  kHz).<sup>77</sup> In the light of this literature study, and considering that the ILP values of commercial magnetic NPs range from 0.15 to 3.12  $\text{nH}\cdot\text{m}^2/\text{kg}_{\text{Fe}}$ ,<sup>78</sup> the magnetic and bioactive nano-heterostructures presented in this work seems to be as efficient, if not better, to similar materials. Other works focused on reviewing bioactive materials for magnetic hyperthermia and provided a complementary and critical overview.<sup>79</sup>

**Table 2** Intrinsic loss power values obtained from the literature for nanosystems based on iron oxides NPs encapsulated in silica or bioactive glass

Reference	Nature of NPs	AMF amplitude (kA/m)	AMF frequency (kHz)	ILP ( $\text{nH}\cdot\text{m}^2/\text{kg}_{\text{Fe}}$ )	
This study	$\gamma\text{-Fe}_2\text{O}_3\text{@SiO}_2\text{-CaO}$	11.9 / 15.9 / 23.9	157 / 304 / 383	2.25 / 2.00 / 1.87	
			493 / 637 / 769	1.71 / 1.67 / 1.69	
Pertou <i>et al.</i> <sup>80</sup>	$\text{Fe}_3\text{O}_4\text{@m-SiO}_2$	8.0	395 / 579 / 796	1.46 / 1.59 / 1.89	
			12.0	395 / 579 / 796	2.13 / 2.29 / 1.83
			16.0	395 / 579 / 796	1.24 / 1.81 / 1.72
Adam <i>et al.</i> <sup>81</sup>	$\text{SPION@m-SiO}_2$ <sup>(a)</sup>	23.9	536.5	2.38	
	$\text{SPION@m-SiO}_2$ <sup>(b)</sup>	23.9	536.5	1.73	
Hurley <i>et al.</i> <sup>82</sup>	$\text{SPION@m-SiO}_2$	19.9	190	2.68	
Gao <i>et al.</i> <sup>83</sup>	$\text{SPION@m-SiO}_2$	19.9	360	2.72	
Moorthy <i>et al.</i> <sup>64</sup>	$\text{Fe}_3\text{O}_4\text{@m-SiO}_2$	14.4	409	1.42	
Nemec <i>et al.</i> <sup>68</sup>	$\gamma\text{-Fe}_2\text{O}_3\text{@SiO}_2$	14.4	471	2.0	
Horny <i>et al.</i> <sup>84</sup>	$\gamma\text{-Fe}_2\text{O}_3\text{@SiO}_2$ <sup>(c)</sup>	10.6	535	1.06	
	$\gamma\text{-Fe}_2\text{O}_3\text{@SiO}_2$ <sup>(d)</sup>	10.6	535	1.37	
Guisasola <i>et al.</i> <sup>67</sup>	$\text{Fe}_3\text{O}_4\text{@m-SiO}_2$	20.1	838	0.5	
		23.9	424 / 550 / 717	0.22 / 0.29 / 0.33	
Kesse <i>et al.</i> <sup>30</sup>	$\gamma\text{-Fe}_2\text{O}_3\text{@SiO}_2\text{-CaO}$	23.9	536.5	0.52	

<sup>(a)</sup> mesoporous silica with stellate pore morphology and <sup>(b)</sup> with worm-like pore morphology  
<sup>(c)</sup> spherical core-shell NPs and <sup>(d)</sup> elongated core-shell NPs

Eventually, the evaluation of SLP in a medium with an increased viscosity is highly recommended to approach *in vivo* conditions (instead of water where particles can move freely).<sup>65</sup> Indeed, inside the body, the nanomaterial will be in contact with viscous fluids or tissues that could affect heat dissipation mechanisms. Agar gel is commonly used to mimic extracellular matrix or tissues depending on its concentration.<sup>71,82,85,86</sup> Here, the SLP values were assessed with a similar procedure as the measurements done in water, but with  $\gamma$ -Fe<sub>2</sub>O<sub>3</sub>@SiO<sub>2</sub>-CaO NPs dispersed in an aqueous solution with 1 %<sub>wt</sub> of agar. The temperature profiles under different AMF conditions are presented in Figure S6 in Supporting Information. Given the low agar concentration, the specific heat capacity of the surrounding medium was taken equal to that of water, and the SLP values were calculated with the same formula. The Table 3 compares the experimental SLP values obtained for different field conditions in water and agar: a loss up to ~ 20 % occurs when NPs are immobilized in the gel. This diminution is consistent with other studies on SPIONs dispersed in viscous media and can be explained by the reduction, or even inhibition, of the Brownian contribution in magnetic heating,<sup>71,82,85,86</sup> as the Brownian relaxation time increases linearly with viscosity (eq. 3).

**Table 3** SLP values of heterostructured NPs dispersed in water and in agar for different field frequency, at fixed amplitude  $H_0 = 23.9$  kA/m

Frequency	SLP in H <sub>2</sub> O (W/g <sub>Fe</sub> )	SLP in 1 % <sub>wt</sub> agar (W/ g <sub>Fe</sub> )	Mean SLP loss
157 kHz	207 ± 3	166 ± 24	19.7 %
383 kHz	407 ± 6	384 ± 4	5.7 %
769 kHz	767 ± 77	678 ± 10	11.6 %

It is important to note that these core-shell NPs still provide efficient heating when immobilized in agar, indicating that Brownian relaxation is not the main source of heat production and that this material is a promising candidate for *in vivo* hyperthermia conditions. This result was expected for SPIONs core size between 14 and 16 nm, where both Brownian and Néel relaxation mechanisms contribute to heat generation.<sup>76</sup>

## Conclusions

Superparamagnetic and bioactive nanometric heterostructures were synthesized by a multistep approach, based on the co-precipitation and sol-gel methods, without hazardous solvents. The control of magnetic NPs size, functionalization and concentration allowed for a successful silica shell encapsulation (Stöber process), without pure silica homogeneous nucleation or excessive magnetic core clustering. Then, the addition of calcium nitrate and a post-synthesis thermal treatment led to the obtention of a bioactive glass shell. Morphological characterizations confirmed that non-aggregated core-shell nanometric particles with low size dispersity (122 ± 12 nm) were synthesized. The SLP values of the  $\gamma$ -Fe<sub>2</sub>O<sub>3</sub>@SiO<sub>2</sub>-CaO NPs (43 – 767 W/g<sub>Fe</sub>) follow Rosensweig's model for magnetic fluids based on the Linear Response Theory in the range of AMF amplitude (11.9 – 23.9 kA/m) and frequency (157 – 769 kHz) studied. The intrinsic loss power (ILP) was calculated at given frequencies by fitting the SLP *versus*  $H_0^2$  curves, method which could be a better way to obtain a single ILP value for any field amplitude, a more relevant value which would also facilitate the comparison with literature. This extensive magnetic hyperthermia study also pointed out that the SLP does not evolve linearly with frequency and so that the ILP values are frequency dependent. Above all, hyperthermia was assessed under clinically relevant AMF parameters (respecting  $H_0 \times f < 5 \cdot 10^9$  A·m<sup>-1</sup>·s<sup>-1</sup>) and in viscous medium to be as close as possible to the medical application. Despite an expected moderately lower heating rate (*ca.* 20 %), the results are promising for magnetic hyperthermia cancer treatment. Furthermore, *in vitro* bioactivity tests and MTT assays after 7 days respectively confirmed the ability to promote HAp growth in SBF and the cytocompatibility of the heterostructures. All these results demonstrated that the  $\gamma$ -Fe<sub>2</sub>O<sub>3</sub>@SiO<sub>2</sub>-CaO NPs presented in this study can be considered as a promising candidate as building block for bone filling material after a tumor resection, to promote bone tissue repair and prevent cancer cells resurgence. Such heterostructured nanoparticles could be directly used as bone fillers (*e. g.* mixed with blood), incorporated in polymeric scaffolds, in hydrogel systems or even shaped as coatings or scaffolds.

## Author contributions

X.K. carried out the NPs synthesis and their morphological and structural characterizations, A.J. performed the cytotoxicity test, and F.P. the magnetic measurements. F.V. carried out all remaining characterizations and studies except ICP-AES measurement and processed all experimental data. C.V. designed the study and was in charge of overall direction and planning. All authors have proofread and given approval to the final version of the manuscript.

## Conflicts of interest

The authors declare no competing financial interests.

## Acknowledgements

The authors acknowledge the support of the French Agence Nationale de la Recherche (ANR) for the Nano-BioMag project under reference ANR-19-CE09-0001. The authors wish to thank Xiangyu Tian for her help in materials synthesis, Christelle Blavignac, Lorraine Novais-Gameiro and Claire Szczepaniak from CICS (UCA) for technical assistance (TEM) and Mhammed Benbakkar from LMV (UCA) for carrying out ICP-AES measurements.

## References

1. Fatima H, Charinpanitkul T, Kim K seon. *Nanomaterials*. 2021;11(5):1203.
2. Freeman AK, Sumathi VP, Jeys L. *Surg (United Kingdom)*. 2015;33(1):34-39.
3. Folkert IW, Devalaraja S, Linette GP, Weber K, Haldar M. *J Bone Miner Res*. 2019;34(10):1780-1788.
4. Baeza A, Arcos D, Vallet-Regí M. *J Phys Condens Matter*. 2013;25(48).
5. Wust P, Hildebrandt B, Sreenivasa G, et al. *Lancet Oncol*. 2002;3(8):487-497.
6. Gazeau F, Lévy M, Wilhelm C. *Nanomedicine*. 2008;3(6):831-844.
7. Ota T, Nishida Y, Ikuta K, et al. *PLoS One*. 2017;12(7):1-16.
8. Gilchrist RK, Medal R, Shorey WD, Hanselman RC, Parrott JC, Taylor CB. *Ann Surg*. 1957;146(4):596-606.
9. Sugimachi K, Kitamura K, Baba K, et al. *Int J Hyperth*. 1992;8(3):289-295.
10. Rao W, Deng ZS, Liu J. *Crit Rev Biomed Eng*. 2010;38(1):101-116.
11. Datta NR, Ordóñez SG, Gaipl US, et al. Vol 41.; 2015:742-753.
12. Takahashi I, Emi Y, Hasuda S, Kakeji Y, Maehara Y, Sugimachi K. *Surgery*. 2002;131(1 SUPPL.):78-84.
13. Issels R. *Onkologie*. 1999;22(5):374-381.
14. Van Der Zee J, González DG, Rhoon GC Van, Dijk JDP Van, Putten WLJ Van. *Lancet*. 2000;355:1119-1125.
15. Harima Y, Nagata K, Harima K, Ostapenko V V., Tanaka Y, Sawada S. *Int J Hyperth*. 2009;25(5):338-343.
16. Dennis CL, Ivkov R. *Int J Hyperth*. 2013;29(8):715-729.
17. Gutiérrez L, Lázaro FJ, Abadía AR, et al. *J Inorg Biochem*. 2006;100(11):1790-1799.
18. Mukherjee S, Liang L, Veiseh O. *Pharmaceutics*. 2020;12(2):147.
19. Jones JR. *Acta Biomater*. 2013;9(1):4457-4486.
20. Hench LL. *New J Glas Ceram*. 2013;3:67-73.

21. Vichery C, Nedelec JM. *Materials (Basel)*. 2016;9(4).
22. Kesse X, Vichery C, Jacobs A, Descamps S, Nedelec JM. *ACS Appl Bio Mater*. 2020;3(2):1312-1320.
23. Hoppe A, Güldal NS, Boccaccini AR. *Biomaterials*. 2011;32(11):2757-2774.
24. Jacobs A, Renaudin G, Forestier C, Nedelec JM, Descamps S. *Acta Biomater*. 2020;117:21-39.
25. Zhang J, Zhao S, Zhu M, et al. *J Mater Chem B*. 2014;2(43):7583-7595.
26. Wang H, Zhao S, Zhou J, et al. *J Mater Chem B*. 2015;3(21):4377-4387.
27. Ohura K, Ikenaga M, Nakamura T, et al. *J Appl Biomater*. 1991;2(3):153-159.
28. Ikenaga M, Ohura K, Yamamuro T, Kotoura Y, Oka M, Kokubo T. *J Orthop Res*. 1993;11(6):849-855.
29. Matsumine A, Kusuzaki K, Matsubara T, et al. *Clin Exp Metastasis*. 2007;24(3):191-200.
30. Kesse X, Adam A, Begin-Colin S, et al. *ACS Appl Mater Interfaces*. 2020;12(42):47820-47830.
31. Boccaccini AR, Erol M, Stark WJ, Mohn D, Hong Z, Mano JF. *Compos Sci Technol*. 2010;70(13):1764-1776.
32. Kailasa SK, Joshi DJ, Kateshiya MR, Koduru JR, Malek NI. *Mater Today Chem*. 2022;23:100746.
33. Ding X, Shi J, Wei J, et al. *Sci Adv*. 2021;7(50).
34. Kang MS, Lee NH, Singh RK, et al. *Biomaterials*. 2018;162:183-199.
35. Demir-Oğuz Ö, Boccaccini AR, Loca D. *Bioact Mater*. 2023;19(March 2022):217-236.
36. Zhao F, Xie W, Zhang W, et al. *Adv Healthc Mater*. 2018;7(16):1-11.
37. Monavari M, Homaeigohar S, Fuentes-Chandía M, et al. *Mater Sci Eng C*. 2021;131:112470.
38. Wang C, Meng C, Zhang Z, Zhu Q. *Ceram Int*. 2022;48(6):7491-7499.
39. Bahremandi-Toloue E, Mohammadalizadeh Z, Mukherjee S, Karbasi S. *Ceram Int*. 2021;(December).
40. Liverani L, Liguori A, Zezza P, et al. *Bioact Mater*. 2022;11(September):230-239.
41. Fiume E, Ciavattini S, Verné E, Baino F. *Materials (Basel)*. 2021;14(11).
42. Vichery C, Maurin I, Bonville P, Boilot JP, Gacoin T. *J Phys Chem C*. 2012;116(30):16311-16318.
43. Li L, Mak KY, Leung CW, et al. *Microelectron Eng*. 2013;110:329-334.
44. Kokubo T, Takadama H. *Biomaterials*. 2006;27(15):2907-2915.
45. Jacobs A, Renaudin G, Charbonnel N, Nedelec JM, Forestier C, Descamps S. *Mater 2021, Vol 14, Page 2393*. 2021;14(9):2393.
46. Julián-López B, Boissière C, Chanéac C, et al. *J Mater Chem*. 2007;17(16):1563-1569.
47. Hergt R, Dutz S, Zeisberger M. *Nanotechnology*. 2010;21(1):015706.
48. Rosensweig RE. *J Magn Magn Mater*. 2002;252(1-3 SPEC. ISS.):370-374.
49. Ozel F, Kockar H, Karaagac O. *J Supercond Nov Magn*. 2015;28(3):823-829.
50. Campelj S, Makovec D, Drofenik M. *J Phys Condens Matter*. 2008;20(20).
51. Srdic V, Mojic B, Nikolic M, Ognjanovic S. *Process Appl Ceram*. 2013;7(2):45-62.
52. Kesse X, Vichery C, Nedelec JM. *ACS Omega*. 2019;4(3):5768-5775.

53. Zheng K, Taccardi N, Beltrán AM, et al. *RSC Adv.* 2016;6(97):95101-95111.
54. Etheridge M, Manuchehrabadi N, Franklin R, Bischof J. In: *Nanoparticle Heat Transfer and Fluid Flow.* ; 2012:97-122.
55. Shokrollahi H. *J Magn Magn Mater.* 2017;426(July 2016):74-81.
56. Li X, Wang X, Hua Z, Shi J. *Acta Mater.* 2008;56(13):3260-3265.
57. Zhang Y, Liu Y, Li M, Lu S, Wang J. *Ceram Int.* 2013;39(6):6591-6598.
58. Wu C, Fan W, Zhu Y, et al. *Acta Biomater.* 2011;7(10):3563-3572.
59. Ur Rahman MS, Tahir MA, Noreen S, et al. *RSC Adv.* 2020;10(36):21413-21419.
60. Sabouri Z, Labbaf S, Karimzadeh F, Baharlou-Houreh A, McFarlane T V., Nasr Esfahani MH. *Biomed Mater.* 2021;16(3).
61. Sharifi E, Bigham A, Yousefiasl S, et al. 2021;2102678.
62. Martínez A, Izquierdo-Barba I, Vallet-Regí M. *Chem Mater.* 2000;12(10):3080-3088.
63. Aguiar H, Serra J, González P, León B. *J Non Cryst Solids.* 2009;355(8):475-480.
64. Santha Moorthy M, Subramanian B, Panchanathan M, et al. *New J Chem.* 2017;41(24):15334-15346.
65. Shah RR, Davis TP, Glover AL, Nikles DE, Brazel CS. *J Magn Magn Mater.* 2015;387:96-106.
66. Guardia P, Di Corato R, Lartigue L, et al. *ACS Nano.* 2012;6(4):3080-3091.
67. Guisasola E, Baeza A, Talelli M, et al. *Langmuir.* 2015;31(46):12777-12782.
68. Nemeč S, Kralj S, Wilhelm C, Abou-Hassan A, Rols MP, Kolosnjaj-Tabi J. *Appl Sci.* 2020;10(20):1-12.
69. Hergt R, Dutz S. *J Magn Magn Mater.* 2007;311(1 SPEC. ISS.):187-192.
70. Johannsen M, Gneveckow U, Taymoorian K, et al. *Int J Hyperth.* 2007;23(3):315-323.
71. De La Presa P, Luengo Y, Multigner M, et al. *J Phys Chem C.* 2012;116(48):25602-25610.
72. Hergt R, Hiergeist R, Hilger I, et al. *J Magn Magn Mater.* 2004;270(3):345-357.
73. Hergt R, Hiergeist R, Zeisberger M, et al. *J Magn Magn Mater.* 2004;280(2-3):358-368.
74. Coral DF, Mendoza Zélis P, Marciello M, et al. *Langmuir.* 2016;32(5):1201-1213.
75. Jović Orsini N, Babić-Stojić B, Spasojević V, Calatayud MP, Cvjetičanin N, Goya GF. *J Magn Magn Mater.* 2018;449:286-296.
76. Fortin JP, Wilhelm C, Servais J, Ménager C, Bacri JC, Gazeau F. *J Am Chem Soc.* 2007;129(9):2628-2635.
77. Zhu Y, Shang F, Li B, et al. *J Mater Chem B.* 2013;1(9):1279-1288.
78. Kallumadil M, Tada M, Nakagawa T, Abe M, Southern P, Pankhurst QA. *J Magn Magn Mater.* 2009;321(10):1509-1513.
79. Sedighi O, Alaghmandfard A, Montazerian M, Bairo F. *J Am Ceram Soc.* 2021;(February):1-25.
80. Pertion F, Tasso M, Muñoz Medina GA, et al. *Appl Mater Today.* 2019;16:301-314.
81. Adam A, Parkhomenko K, Duenas-Ramirez P, et al. *Molecules.* 2021;26(4):971.
82. Hurley KR, Ring HL, Etheridge M, et al. *Mol Pharm.* 2016;13(7):2172-2183.

83. Gao Z, Ring HL, Sharma A, et al. *Adv Sci.* 2020;7(4).
84. Horny MC, Gamby J, Dupuis V, Siaugue JM. *Nanomaterials.* 2021;11(1):1-15.
85. Shah RR, Dombrowsky AR, Paulson AL, Johnson MP, Nikles DE, Brazel CS. *Mater Sci Eng C.* 2016;68:18-29.
86. Nemati Z, Alonso J, Rodrigo I, et al. *J Phys Chem C.* 2018;122(4):2367-2381.